

Dual-Site Cation Codoping Strategies Mitigating H₂–H₃ Phase Transition for Cycle Stable Nickel-Rich Layered Oxide Cathodes in Lithium Batteries

Abhishek Kumar, Uttam Kumar Goutam, Ranabrata Mazumder, and Partha Saha*

Layered Ni-rich transition metal oxide cathodes ($\text{LiNi}_{0.65}\text{Mn}_{0.1}\text{Co}_{0.25}\text{O}_2$ -NMC) continue to dominate the market owing to the demand for high-energy-density lithium-ion batteries. However, these cathodes suffer from rapid capacity and voltage decay during high voltage operation (≤ 4.5 V) due to unavoidable cation disorder ($\text{Li}^+/\text{Ni}^{2+}$) and $\text{H}2 \rightarrow \text{H}3$ phase transformation, inflicting structural instability. Herein, dual-site cation doping using Mg^{2+} in Li 3a sites and Zr^{4+} in transition metal-T_M (preferably Ni sites) 3b sites is shown to preserve structure at high voltage, improving capacity retention and voltage fade. The Rietveld refinement of diffraction data shows that cation disorder reduced from $\approx 11\%$ (NMC) to $\approx 2.9\%$ (ZrMg-NMC) with a low

defect formation energy (ΔE) of NMC (≈ 202.33 meV), favoring the formation of antisite defects. Cyclic voltammogram confirms that codoping prevents the $\text{H}2 \rightarrow \text{H}3$ transformation at high voltage (≤ 4.5 V), reflected in better capacity retention (ZrMg-NMC: $\approx 85\%$, vs. NMC: $\approx 51\%$ at 200 cycles during cycling at 0.1C) and sluggish average voltage fading rate (ZrMg-NMC: ≈ 0.12 mV/cycle, vs. NMC: ≈ 0.22 mV/cycle). The remarkable performance improvement by Zr-Mg codoping in NMC stems from preventing oxygen migration to the surface, dissuading rock salt phase formation, and stronger Ni–O and Ni–T_M bond lengths, immensely helping to retain structural stability during charging up to 4.5 V.

1. Introduction

Rechargeable Li-ion batteries (LIBs) have emerged as attractive power sources for electrical energy storage devices.^[1–5] Since the last decade, significant efforts have been made to enhance the performance of Ni-rich layered oxide cathodes for use in LIBs.^[6] Among various candidates, $\text{Li}_x\text{Ni}_y\text{Co}_z\text{Mn}_{1-y-z}\text{O}_2$ (NMC; $0 < x \leq 1.2$, $0.6 < y < 1$, $0 < z < 0.4$)-based layered oxide cathodes have emerged as materials of choice, offering higher cell voltage and sp. Capacity.^[7,8] Liu et al.^[9] reported that Ni-ions are electrochemically active and contribute to higher capacity, while Co-ions enhance the rate capability, and Mn-ions provide structural stability.^[9] However, the capacity and voltage fading generally occur in high voltage (4.2–4.5 V) Ni-rich NMC cathodes owing to phase transformation-induced structural instability, promoting cathode electrolyte interphase (CEI) formation and preventing facile Li^+ -ion movements, deteriorating cell performance.^[10]

The main reasons behind the capacity fading of Ni-rich NMC-based cathodes are the structure instability during charging at high voltage, formation of residual lithium compounds (Li_2CO_3 ,

LiOH), $\text{Li}^+/\text{Ni}^{2+}$ cation mixing, side reaction, metal–oxygen bond instability, rock salt phase formation, metal ion dissolution, and particles microcracking.^[11,12] It has generally been observed that Ni-rich NMC cathodes undergo a series of phase transformations starting from the initial hexagonal phase (H1) to monoclinic (M) phase, followed by second hexagonal (H2) and third hexagonal (H3) phases during charging above 4.2 V. Among all, the H2 to H3 phase transformation inflicts severe structural damage owing to rapid shrinkage of lattice parameters and unit cell volume, accompanied by lattice oxygen release and cathode active particles microcracking.^[13,14] Besides, during charging Li-ions deintercalation followed by Ni^{2+} oxidation to smaller $\text{Ni}^{3+}/\text{4}^+$ ions (ionic radii: Ni^{3+} : 0.056 nm, and Ni^{4+} : 0.053 nm) inadvertently leads to irreversible phase transformation of layered ($\text{R}\bar{3}m$) to disordered spinel ($\text{Fd}\bar{3}m$) and eventually ionically insulating NiO-type rock salt phase ($\text{Fm}\bar{3}m$) formation at the surface of cathode particles.^[15] The mechanical strain accompanied by Ni-rich NMC cathodes during the periodic charge–discharge process leads to continuous fluctuation of lattice constants, contributing to exposing new surfaces prone to side reactions and CEI formation.^[16,17] Moreover, $\text{Li}^+/\text{Ni}^{2+}$ cation mixing due to the partial interchange of occupancy of Li^+ on 3a sites (000) and Ni^{2+} on 3b sites (0 0 1/2) during high-temperature synthesis and battery cycling also contributes to structural instability.^[18,19]

Various research groups have proposed a series of strategies to address the aforementioned drawbacks, including surface coating, cation doping, and the addition of additives to electrolytes.^[20,21] Among these, cation doping has been recognized as an effective approach for enhancing electrochemical properties. By facilitating charge compensation, cation substitution can balance the valence states of both oxygen and transition metals.

A. Kumar, R. Mazumder, P. Saha
Department of Ceramic Engineering
National Institute of Technology
Rourkela, Odisha 769008, India
E-mail: sahap@nitrl.ac.in

U. K. Goutam
Technical Physics Division
Bhabha Atomic Research Centre
Mumbai 400085, India

 Supporting information for this article is available on the WWW under <https://doi.org/10.1002/batt.202500262>

Additionally, it modifies the interlayer spacing between lithium-ion and transition metal layers, thereby improving electronic and lithium-ion conductivity while enhancing the overall stability of bulk materials.^[22,23] Therefore, the single or multiple doping of cations can be viable options using divalent (Mg^{2+} , Zn^{2+} , Cu^{2+}), trivalent (Al^{3+} , Fe^{3+} , Cr^{3+}), tetravalent (Zr^{4+} , Ti^{4+} , Si^{4+}), pentavalent (Nb^{5+} , Ta^{5+}) cations, and their combination thereof.^[24] The doping with aliovalent or multivalent cations in Ni^{2+} and Li^{+} sites can improve the ionic conductivity, preventing migration of Ni^{2+} ions to the Li sites, decreasing antisite defects, leading to enhanced structural stability, and eventually strengthening T_M -ion bond strength by inhibiting oxygen release during cycling.^[25] Wang et al.^[26] reported that 0.01 mol of Mg^{2+} and 0.01 mol of Ti^{4+} codoping in NMC can effectively broaden the Li-ions diffusion channels, mitigating the structural collapse and unfavorable phase transformation to some extent. The doping concentration also plays a significant role in the structural and electrochemical properties. Earlier work elucidated that 0.01 mol of dopant concentration is optimal, effectively enhancing the Li-ion kinetics by stabilizing the crystal structure.^[27,28]

In this work, we aim to study the synergistic effect of Zr^{4+} and Mg^{2+} codoping in a Ni-rich NMC cathode with a chemical formula $LiNi_{0.65}Mn_{0.1}Co_{0.25}O_2$, enhancing the structural and electrochemical properties. It has been shown that the Zr^{4+} cations with higher valence substitutes in the transition metal (Ni, Mn, or Co) 3b sites (0 0 1/2), broadening the interlayer spacing, reducing the oxygen vacancies, suppressing the side reactions (nonequilibrium diffusion reactions at the interface) and simultaneously enhancing the Ni–O bond strength in the NMC-based cathode.^[29] Simultaneously, Mg^{2+} ions preferentially substitute into Li 3a sites (000) due to similar ionic radii, yielding a pillaring effect by reducing the O_2 – O_2 repulsion force and stabilizing the overall lattice structure during (de)lithiation.

2. Results

The powder diffraction data (Figure 1a) of as-prepared samples show the formation of rhombohedral phase (ICDD No. 98-011-1904) with three major Bragg reflections from $\approx 18.65^\circ$, $\approx 36.50^\circ$, and $\approx 44.24^\circ$ corresponding to the (003), (101), and (104) planes. The samples crystallized into an ordered rock salt structure akin to α -NaFeO₂ (space group $R\bar{3}m$). The clear splits of the $I_{(006)}/I_{(102)}$ and $I_{(108)}/I_{(110)}$ doublets corroborate that a well-ordered layered structure was formed.^[15,23,28,30] However, the $I_{(003)}$ diffraction peak of doped samples shifted slightly ($\approx 0.06^\circ$) to a lower Bragg's angle (Figure 1b) compared to the pristine, indicating an expansion in the unit cell volume.^[27] The Zr^{4+} ions with larger ionic radii of (0.74 Å) substitute in the 3b transition metal (T_M) sites, enlarging the interlayer spacing, reducing the oxygen vacancies, and suppressing the side reactions.^[26,31] The theoretical calculation performed by Schipper et al.^[32] showed that Zr^{4+} ions have the highest preference for Ni sites ($E_{subs} = -1.82$ eV per dopant), followed by Co sites ($E_{subs} = -1.80$ eV per dopant) and Mn sites ($E_{subs} = -1.26$ eV per dopant) supports our analysis. On

the contrary, the doping of 0.01 mol of Mg^{2+} ions (0.72 Å) ostensibly segregates into the Li^{+} sites, providing the “pillaring effect” by reducing the O_2 – O_2 repulsive force and suppressing the Li^{+}/Ni^{2+} antisite defects by pushing out the Ni^{2+} (0.69 Å) from the Li^{+} sites.^[26,33] The synergistic effect of Zr^{4+} and Mg^{2+} codoping into the NMC lattice bodes well ameliorating the interlayer spacing and mitigating the Li^{+}/Ni^{2+} cation disorder (Figure 2). Additionally, the codoping can improve the facile lithiation/delithiation owing to the ease of Li^{+} ions migration between [TMO₂] layers and stabilizing the lattice structure to improve cyclability.

The Rietveld refinement Figure 1c-f was conducted using the FullProf software, and the refined cell parameters of NMC, Zr-NMC, Mg-NMC, and ZrMg-NMC are shown in Table S1, Supporting Information. The lithium and T_M -ions are octahedrally coordinated with oxygen in the ABCABC stacking sequence. Rietveld refinement shows that Zr^{4+} was successfully substituted in the Ni 3b sites (0 0 1/2), and Mg^{2+} into Li 3a sites (000). The calculated unit cell parameters a and c of the samples show similar trends reported in the literature.^[34,35] The c/a and $I_{(003)}/I_{(104)}$ ratios indicate the extent of Ni^{2+} cation mixing in the lithium sites (Ni_{Li}) (Figure 1g). Usually, the c/a ratio should be above 4.9, and the $I_{(003)}/I_{(104)}$ ratio of integral intensities must be greater than 1.2 to satisfy the criteria of low cation disorder.^[9,36] The c/a and $I_{(003)}/I_{(104)}$ ratio of NMC were found ≈ 4.948 and ≈ 1.06 , respectively, whereas c/a and $I_{(003)}/I_{(104)}$ ratio of ZrMg-NMC were ≈ 4.964 and ≈ 1.55 , respectively (see Table 1). Therefore, the extent of Li^{+}/Ni^{2+} cation mixing in NMC, Zr-NMC, Mg-NMC, and ZrMg-NMC was determined $\approx 11\%$, $\approx 7.3\%$, $\approx 6.8\%$, and $\approx 2.9\%$, respectively, indicating that gradual doping of Zr and Mg-ions decreased the cationic disorder, and the unit cell volume steadily increased (Table S1, Supporting Information). Further, the antisite defect concentration ($C_{antisite}$), which is the proportion of Ni_{Li} and Li_{Ni} mutual defects, was calculated following the method proposed by Yin et al.^[37] $C_{antisite} = (0.2423 \times [\text{amount of } Ni^{2+}] + 0.01808) \times [\text{total amount of Ni}]$. The $C_{antisite}$ of NMC, Zr-NMC, Mg-NMC, and ZrMg-NMC was found 0.029, 0.023, 0.022, and 0.016, respectively. The energy associated with defect formation (ΔE), from the proportion of Ni-ions in 3a and 3b sites was calculated using Equation (1)

$$\frac{\% \text{ of Ni on Li(3a)sites}}{\% \text{ of Ni on Ni(3b)sites}} = e^{-\Delta E / K_B T} \quad (1)$$

Here, the percentage of Ni on Li(3a) sites and Ni on Ni(3b) sites is the percentage of cation mixing and 100 - % cation mixing, respectively. The ΔE of NMC, Zr-NMC, Mg-NMC, and ZrMg-NMC was determined ≈ 202.33 , ≈ 245.95 , ≈ 253.33 , and ≈ 339.78 meV, respectively. The highest defect formation energy (ΔE) of codoped NMC among four samples indicates the ZrMg-NMC sample was highly resistant toward forming the antisite defects, rendering a stable structure with strong Ni–O bond preventing structural collapse. The R factor, expressed as $(I_{(006)} + I_{(102)})/I_{(101)}$, defines the hexagonal ordering in which a lower R factor is synonymous with better hexagonal ordering.^[38,39] The R factor of NMC and ZrMg-NMC was ≈ 0.57 and ≈ 0.51 , respectively, demonstrating that the ZrMg-NMC sample possesses better hexagonal ordering. The Williamson–Hall analysis was carried out to determine the crystallite size and the lattice strain of the calcined

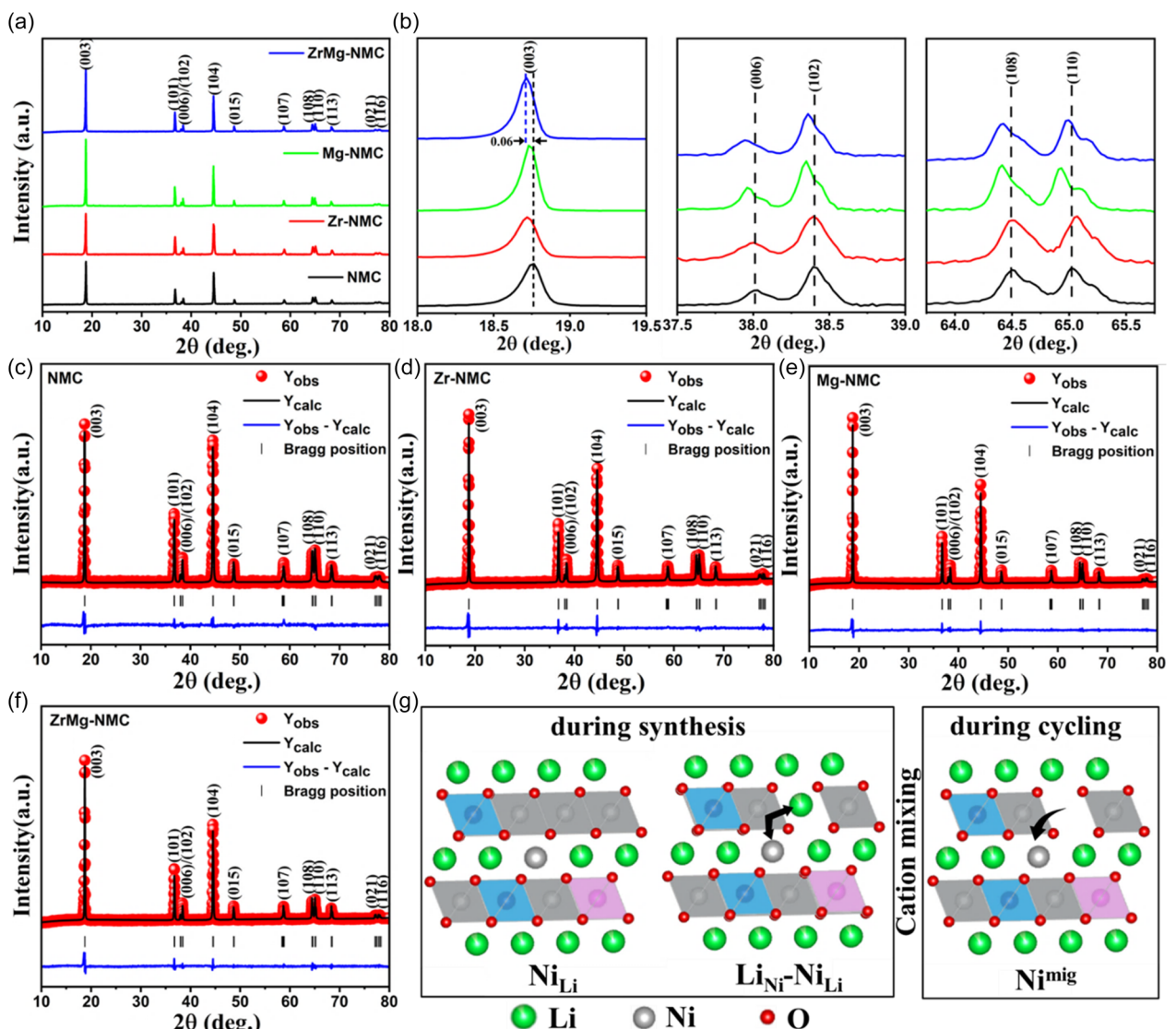


Figure 1. a) X-ray diffraction pattern, b) the corresponding enlarged portion of $I_{(003)}$, $I_{(006)}$, $I_{(102)}$, $I_{(108)}$ and $I_{(110)}$ reflection. c-f) Rietveld refinement analysis of NMC, Zr-NMC, Mg-NMC, and ZrMg-NMC, respectively, and g) schematic diagrams representing the cation mixing during synthesis and cycling.

samples (Figure S1, Supporting Information). The crystallite size ($D \approx 27.42$ nm) and lattice strain ($\epsilon \approx 0.003\%$) of ZrMg-NMC were comparatively less than NMC ($D \approx 33.14$ nm, $\epsilon \approx 0.041\%$), further suggesting the beneficial effect of codoping. All the above findings are in favor of codoping; however, thermal stability remains an important concern for Ni-rich layered oxide cathodes fulfilling the safety criteria during high-temperature operations in Li-ion cells. Therefore, the temperature-dependent magnetic moment was performed by vibrating sample magnetometer (VSM) analysis, revealing that ZrMg-NMC can significantly inhibit the oxygen charge transfer and remain thermally stable (Figure S2, Supporting Information for details).

The field emission scanning electron microscopy (FESEM) image Figure in S3a-d, Supporting Information, shows the secondary particle morphology, confirming that the samples consist of well-formed spherical agglomerates composed of nanosized primary particles. The corresponding particle size distribution (PSD) was fitted with a Gaussian profile, and the median particle

size (D_{50}) for ZrMg-NMC was $\approx 0.78 \pm 0.01$ μm , a slight decrease in particle size compared to the NMC ($\approx 0.47 \pm 0.01$ μm). The X-ray mapping and energy dispersive spectrometry (EDS) spectra, as shown in Figure S3e-k, Supporting Information, confirmed the presence of Ni, Co, Mn, Zr, and Mg distributed uniformly in the ZrMg-NMC. The microstructural analysis demonstrates that Zr and Mg are present in the NMC lattice. The stoichiometric ratio of Ni: Co: Mn: Zr: Mg for the doped sample matched closely with the anticipated value (Figure S3(l), Supporting Information). The bright field transmission electron microscope (TEM) shows high-resolution images of NMC and ZrMg-NMC samples at the nano-scale, illustrating the size and shape of primary particles, as shown in Figure 3a,b. The PSD follows the Gaussian profile, and the median particle size (D_{50}) of NMC and ZrMg-NMC was estimated $\approx 16.4 \pm 1.4$ and $\approx 6.5 \pm 1.2$ nm, respectively. The high-resolution transmission electron microscope (HR-TEM) images reveal that ZrMg-NMC sample formed a layered rhombohedral phase ($R\bar{3}m$) along with minor spinel phases ($Fd\bar{3}m$), however, NMC possessed

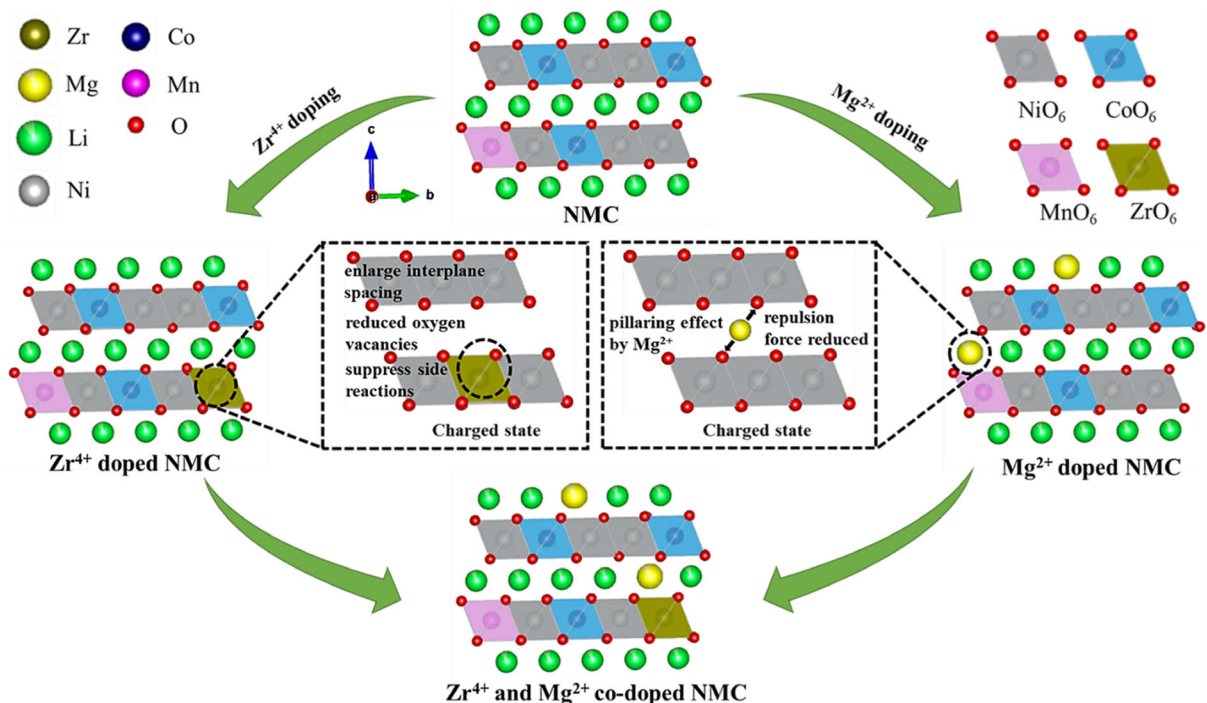


Figure 2. Schematic diagram represents the structural change due to Zr⁴⁺ and Mg²⁺ codoping in NMC cathode.

an additional rock salt cubic ($Fm\bar{3}m$) phase. The interplanar spacing calculated from the lattice fringes reveals that ZrMg-NMC has a higher interplanar spacing of ≈ 0.31 nm compared to ≈ 0.21 nm for NMC (Figure 3c,d). The TEM results were in sync with the X-ray diffraction (XRD) data shown in Figure 1. The fast Fourier transform (FFT) of HR-TEM images analyzed from the selected area in Figure 3c,d, indicates the bulk of the particles exhibit rhombohedral $R\bar{3}m$ phase for NMC sample (Figure 3c1, region I), while spinel-like $Fd\bar{3}m$ and cubic $Fm\bar{3}m$ (area drawn by a yellow dash) indicate the eventual presence of rock salt phase, denoting $(1\bar{1}\bar{1})$ planes of NiO-type structure (Figure 3c2, region 2; Figure 3c3, region 3). Generally, the NMC-type cathode particle surface exhibits a combination of structural defects, that is, distortion of the layer structure, stacking faults, and dislocations.^[40,41] The additional spinel-like and rock salt phase formation is attributed to the Li⁺/Ni²⁺ cation mixing ($\approx 11\%$) in NMC. The presence of rock salt phase obstructs the Li⁺-ion mobility and increases charge

transfer resistance during cycling.^[42,43] On the contrary, the corresponding FFT patterns of ZrMg-NMC demonstrate that particle surface maintained a rhombohedral structure with a slight transformation into a spinel-like cubic phase (Figure 3d1, Region 1; Figure 3d2, Region 2) owing to low Li⁺/Ni²⁺ cation mixing ($\approx 2.9\%$). The crystal structure of different phases is shown in Figure 3e. The unit cell represents the rhombohedral ($R\bar{3}m$), spinel ($Fd\bar{3}m$) and rock salt cubic ($Fm\bar{3}m$) phases, respectively.

The X-ray photoemission spectroscopy (XPS) determines the surface chemical composition and valence states of T_M elements. Figure S4a–c, Supporting Information, shows the survey spectra and corresponding Mn 2p and Co 2p peaks of NMC, Zr-NMC, Mg-NMC, and ZrMg-NMC. Figure 4a shows that Ni 2p peaks at ≈ 853.9 eV for Ni 2p_{3/2} and ≈ 871.7 eV for Ni 2p_{1/2} with two satellite peaks at ≈ 860.2 and ≈ 878.1 eV, respectively.^[28,44,45] The Ni 2p_{3/2} spectra were decoupled into two peaks at ≈ 853.4 and ≈ 854.9 eV, respectively, ascribed to Ni²⁺ and Ni³⁺. Interestingly, ZrMg-NMC (Figure 4a) reveals a higher Ni³⁺ content of $\approx 55.6\%$ compared to NMC of $\approx 49.8\%$, that can be related to lower Li⁺/Ni²⁺ cation mixing in the former. The higher amount of Ni²⁺ in NMC is detrimental and may lead to the site exchange with Li in 3a sites (000) and transition metal in 3b sites (0 0 1/2), giving rise to antisite defects during galvanostatic charging. The two peaks of O 1s correspond to the binding energy of ≈ 527.3 and ≈ 529.7 eV (Figure 4b) related to the lattice oxygen (O_{lattice}) and the chemisorbed oxygen (O_{adsorbed}) of residual surface impurities (LiOH, Li₂CO₃, and LiHCO₃).^[23,26] The chemisorbed oxygen originating from residual surface impurities may lead to the decomposition of the active particles through HF attack, oxygen evolution, and lithium plating.^[46] The higher O_{lattice} content of $\approx 23.8\%$ for ZrMg-NMC compared to $\approx 5.1\%$ O_{lattice} content for NMC validates that Zr⁴⁺ and

Table 1. The crystallographic data obtained from the Rietveld refinement analysis.

Parameters	NMC	Zr-NMC	Mg-NMC	ZrMg-NMC
a [Å]	≈ 2.870	≈ 2.871	≈ 2.871	≈ 2.872
c [Å]	≈ 14.205	≈ 14.219	≈ 14.237	≈ 14.256
c/a	4.948	4.953	4.959	4.964
Li _{3a}	≈ 0.89	≈ 0.927	≈ 0.932	≈ 0.971
Ni _{3a}	≈ 0.11	≈ 0.073	≈ 0.068	≈ 0.029
I ₍₀₀₃₎ /I ₍₁₀₄₎	1.06	1.27	1.54	1.55
Crystallite Size [nm]	≈ 33.14	≈ 24.46	≈ 26.33	≈ 27.42
Strain	0.00041	0.00027	-0.00014	0.000029

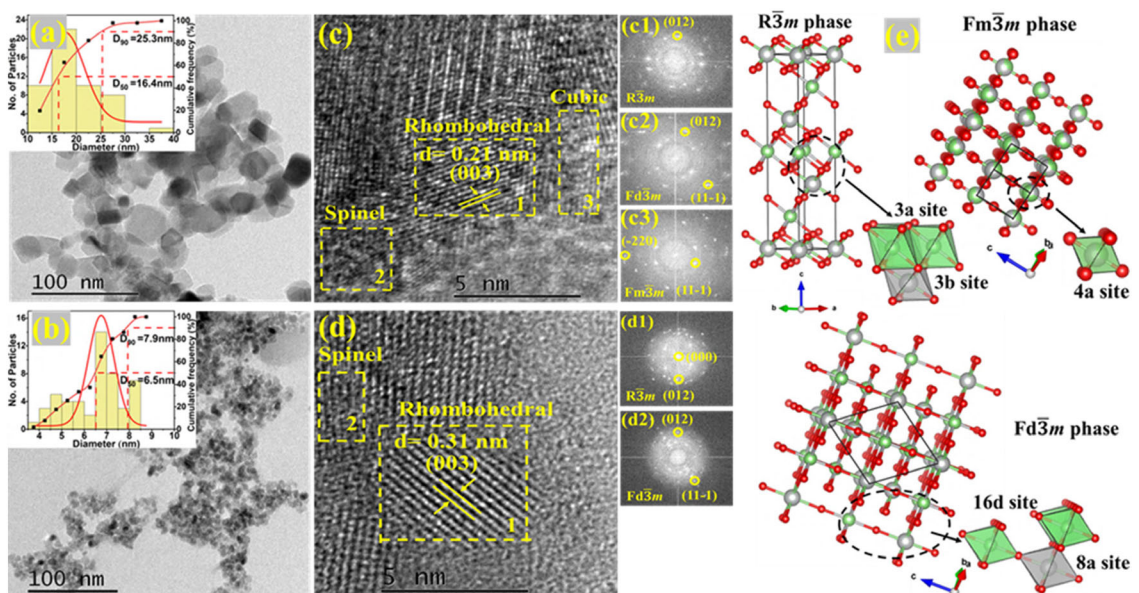


Figure 3. Bright-field TEM images with PSD (inset), and HR-TEM images showing lattice fringes of different phases and corresponding FFT patterns of a,c) NMC and b,d) ZrMg-NMC, and e) crystal structure of different phases.

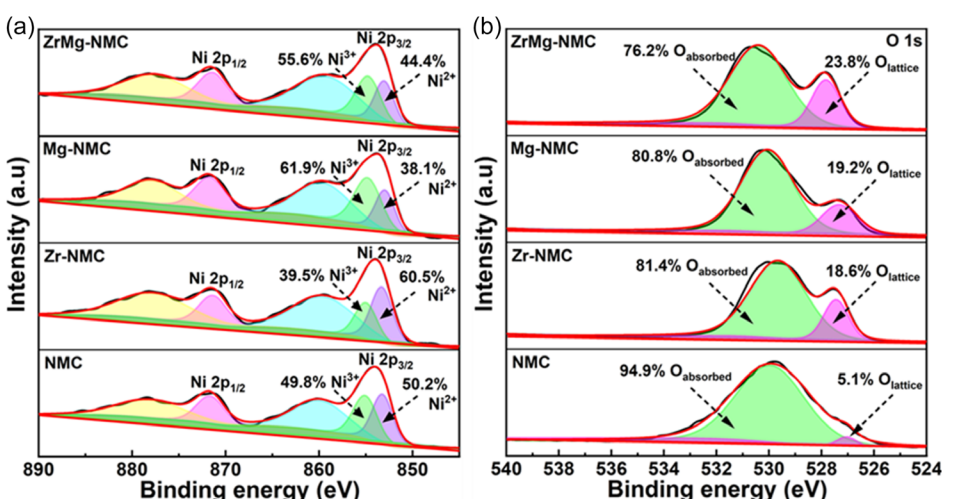


Figure 4. XPS spectra of a) Ni 2p and b) O 1s of NMC, Zr-NMC, Mg-NMC, and ZrMg-NMC.

Mg²⁺ codoping in NMC prevents oxygen migration to the surface by forming the stronger T_M—O bonds. The XPS spectra at ≈ 182.1 and ≈ 1302.9 eV attribute to Zr 3d_{3/2} and Mg 1s, respectively, for the ZrMg-NMC sample (Figure S4d,e, Supporting Information).

The cyclic voltammetry (CV) of the NMC and ZrMg-NMC cathodes was performed at a scan rate of 0.05 mVs^{-1} within the $3\text{ V} \leq E \leq 4.2\text{ V}$ potential window, as shown in Figure 5a,b. The NMC shows the anodic peaks at ≈ 3.84 and ≈ 4.15 V corresponding to hexagonal to monoclinic ($\text{H1} \rightarrow \text{M}$) and monoclinic to hexagonal ($\text{M} \rightarrow \text{H2}$) phase transformation during the delithiation process, respectively.^[28] On the contrary, ZrMg-NMC shows a single anodic peak at ≈ 3.87 V, that corresponds to $\text{H1} \rightarrow \text{M}$ phase transformation, with no sign of $\text{M} \rightarrow \text{H2}$ phase transition, thereby preventing unfavorable phase transformation and rapid capacity fade during electrochemical cycling. The cathodic reaction of

NMC displayed two pairs of peaks (Figure 5a) with a potential difference of $\approx 0.07\text{ V}$ between 1st ($\approx 3.64\text{ V}$) and 2nd peak ($\approx 3.57\text{ V}$) during $\text{M} \rightarrow \text{H1}$ phase transformation, indicating structure instability. On the contrary, ZrMg-NMC showed excellent reversibility with a single cathodic peak at $\approx 3.67\text{ V}$ (Figure 5b) corresponding to $\text{M} \rightarrow \text{H1}$ phase transformation, with a potential difference of merely $\approx 0.03\text{ V}$ evident between two consecutive anodic peaks, suggesting structural superiority. It is noteworthy that the potential hysteresis (ΔV) between anodic and cathode peaks plays an important role in representing polarization and electrochemical reversibility. During the 2nd cycle onwards, the ΔV of $\approx 0.17\text{ V}$ was evident for the ZrMg-NMC cathode, lower than the ΔV of $\approx 0.2\text{ V}$ for the NMC cathode, suggesting codoping in the former minimizes polarization, enhancing the electrochemical reversibility.

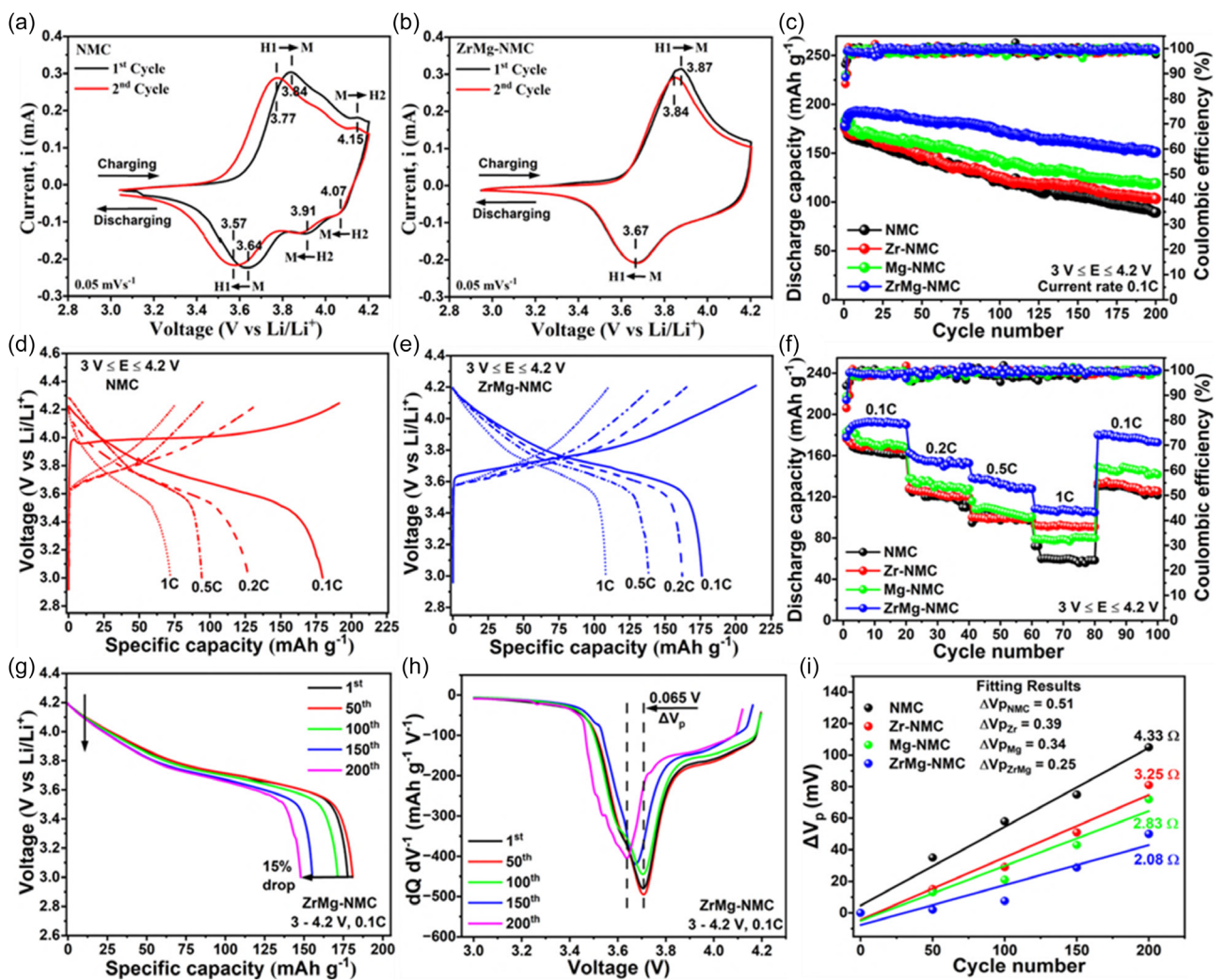


Figure 5. Cyclic voltammograms of a) NMC, b) ZrMg-NMC, and c) cycle performances of the assembled cells. Galvanostatic charge–discharge profile at different rates of d) NMC, e) ZrMg-NMC, and f) rate capability of NMC, Zr-NMC, Mg-NMC, and ZrMg-NMC. g,h) Selected discharge profiles and their corresponding $dQ\,dV^{-1}$ versus voltage curves of ZrMg-NMC. i) Estimated relative voltage fading rate (ΔV_p) plots of the plateau voltages during cycling within $3\text{ V} \leq E \leq 4.2\text{ V}$ potential window.

The cycling performance of NMC, Zr-NMC, Mg-NMC, and ZrMg-NMC was evaluated in 2032-type coin half cells up to 200 cycles within the $3\text{ V} \leq E \leq 4.2\text{ V}$ potential window at 0.1C rate (Figure 5c). The initial discharge capacity of the NMC cathode was $\approx 179\text{ mAh g}^{-1}$ with a capacity retention of $\approx 68\%$ after 100 cycles and $\approx 51\%$ after 200 cycles. On the contrary, Zr-NMC and Mg-NMC demonstrated higher capacity retention of $\approx 59\%$ and 65% , respectively, after 200 cycles, which can be attributed to the fact that Mg^{2+} -ions stabilize the lattice and Zr^{4+} -ions broaden the interplanar spacing, facilitating Li^{+} -ions diffusion during the lithiation/delithiation process.^[26,47] Further, with Zr^{4+} and Mg^{2+} codoping, the initial discharge capacity was $\approx 178\text{ mAh g}^{-1}$ with a capacity retention of $\approx 96\%$ after 100 cycles and $\approx 85\%$ after 200 cycles, demonstrating superior performance (see details sp. capacity comparison in Table S2, Supporting Information). The activation process is evident during initial cycling for ZrMg-NMC, and the highest discharge capacity was observed $\approx 191\text{ mAh g}^{-1}$ at 10th cycle, and based on that, the capacity retention was $\approx 90\%$ after 100 cycles and $\approx 79\%$ after

200 cycles, respectively. Figure 5d–f shows the comparison of the galvanostatic charge–discharge profile at various C-rates between NMC and ZrMg-NMC and rate capabilities performed at 0.1C to 1C within the $3\text{ V} \leq E \leq 4.2\text{ V}$ potential window. Though NMC provides a discharge capacity of $\approx 179\text{ mAh g}^{-1}$ at 0.1C, the capacity fades dramatically with increasing the C-rates (≈ 127 , ≈ 94 , and $\approx 72\text{ mAh g}^{-1}$ at 0.2C, 0.5C, and 1C, respectively). However, ZrMg-NMC shows a better rate performance (≈ 162 , ≈ 138 , and $\approx 108\text{ mAh g}^{-1}$ at 0.2C, 0.5C, and 1C, respectively) with the highest capacity retention, demonstrating the beneficial effect of Zr^{4+} and Mg^{2+} codoping. The rate performance of Zr-NMC and Mg-NMC was in-between NMC and ZrMg-NMC cathodes, indicating that individual doping can elevate the performance, however, codoping delivers superior performance.

The selected discharge profiles and the corresponding differential capacity ($dQ\,dV^{-1}$) versus voltage (V) plots of NMC, Zr-NMC, Mg-NMC, and ZrMg-NMC are illustrated in Figure S5, Supporting Information, and Figure 5g,h delineate the voltage plateau and corresponding cathodic peaks (first derivative) during the

galvanostatic cycling. The slight fluctuation in the 1st cycle discharge capacity is ascribed to the effect of Mg^{2+}/Zr^{4+} doping in the samples, which remain virtually inert throughout the electrochemical cycling. However, the drop in specific capacity for the NMC, Zr-NMC, Mg-NMC, and ZrMg-NMC was $\approx 49\%$, $\approx 41\%$, $\approx 35\%$, and $\approx 15\%$, respectively, after 200 cycles. The ZrMg-NMC exhibits the minimum capacity and voltage fade with the increasing cycles compared to NMC. The voltage drops at the reaction plateau (corresponds to peaks of dQ/dV^{-1} vs. V plot) of NMC, Zr-NMC, Mg-NMC, and ZrMg-NMC were ≈ 96 , ≈ 81 , ≈ 72 , and ≈ 65 mV, respectively, between 1st and 200th cycles. The voltage drop is generally associated with the loss of the electrochemical reactivity of the Ni^{2+} ions, which migrate into the Li sites during cycling, coupled with the occurrence of the irreversible phase transformation.^[23,48] Therefore, the minimal fall in plateau voltage reveals the suppressed cell resistance and improved interfacial properties in the ZrMg-NMC. The relative voltage fading rate (ΔV_p) was determined and compared in Figure 5i to further evaluate the voltage drop and the cell resistance upon cycling. The estimated ΔV_p determined from the slope of extrapolated curves of NMC, Zr-NMC, Mg-NMC, and ZrMg-NMC was ≈ 0.51 , ≈ 0.39 , ≈ 0.34 , and ≈ 0.25 mV, and the corresponding resistance growth was ≈ 4.33 , ≈ 3.25 , ≈ 2.83 , and $\approx 2.08 \Omega$, respectively. Importantly, ZrMg-NMC exhibits the slowest voltage fading rate and resistance growth, suggesting structural stability.

To further understand the electrochemical performance and stability of cathodes, NMC, Zr-NMC, Mg-NMC, and ZrMg-NMC were cycled within a higher cutoff voltage ($3 \leq V \leq 4.5$ V) (Figure S6a, Supporting Information). The discharge capacity, coulombic efficiency, and capacity retention of NMC, Zr-NMC, Mg-NMC, and ZrMg-NMC are mentioned in Table S2, Supporting Information. The 1st cycle discharge capacity of the NMC was $\approx 176 \text{ mAhg}^{-1}$ with a capacity retention of $\approx 48\%$ after 200 cycles. However, ZrMg-NMC cathodes showed 1st cycle discharge capacity of $\approx 169 \text{ mAhg}^{-1}$ with a capacity retention of $\approx 65\%$ after 200 cycles. Surprisingly, Zr-NMC, although displayed poor 1st cycle discharge capacity ($\approx 138 \text{ mAhg}^{-1}$), exhibits slightly improved capacity retention ($\approx 69\%$) after 200 cycles. The rate performance (Figure S6b, Supporting Information) of electrodes shows that capacity fades dramatically for NMC with increasing C-rates (≈ 176 , ≈ 115 , ≈ 86 , and $\approx 65 \text{ mAhg}^{-1}$ at 0.1C, 0.2C, 0.5C, and 1C, respectively) whereas ZrMg-NMC shows a better rate performance (≈ 169 , ≈ 125 , ≈ 97 , and $\approx 76 \text{ mAhg}^{-1}$ at 0.1C, 0.2C, 0.5C, and 1C, respectively) along with highest capacity retention even during cycling at higher potential window of $3 \leq V \leq 4.5$ V.

Further, CV was carried out between $3 \leq V \leq 4.5$ V, and NMC shows three pairs of anodic peaks corresponding with hexagonal to monoclinic ($H1 \rightarrow M$), monoclinic to hexagonal ($M \rightarrow H2$), and hexagonal to hexagonal ($H2 \rightarrow H3$) phase transformation. However, ZrMg-NMC shows no sign of high voltage $H2 \rightarrow H3$ phase transformation during the charging process (Figure S6c,d, Supporting Information). The $H2 \rightarrow H3$ phase transition appears at ≈ 4.41 V for NMC during charging, causing structural instability. The $H2 \rightarrow H3$ phase transition invokes unit cell volume and lattice parameter shrinkage, leading to micro-crack generation in cathode active particles concomitant with rapid capacity decay in NMC.^[15,28] On the contrary, the ZrMg-NMC cathode prevents

unfavorable $H2 \rightarrow H3$ phase transformation and rapid capacity decay even at a higher cutoff voltage of ≈ 4.5 V. Importantly, during 2nd cycle, ZrMg-NMC shows a lower potential hysteresis ($\Delta V \approx 0.13$ V) than that of NMC ($\Delta V \approx 0.2$ V) for $H1 \rightarrow M$ redox peaks, revealing that codoping can be effective to minimize polarization at higher cutoff voltage. Importantly, the $H2 \rightarrow H3$ and $M \rightarrow H2$ phase transformations of NMC and ZrMg-NMC cathodes, respectively, were completely absent during cycling within $3 \leq V \leq 4.2$ V (Figure 6a,b). Overall, ZrMg-NMC prevents $H2 \rightarrow H3$ and $M \rightarrow H2$ phase transformation during cycling within $3 \leq V \leq 4.2$ V, preserving the structural integrity.

Galvanostatic cycling results show that ZrMg-NMC cathode delivered higher sp. capacity while cycling within $3 \leq V \leq 4.2$ V (Figure 6c) and capacity retention ($\approx 96\%$ after 100 cycles, $\approx 85\%$ after 200 cycles). However, the capacity retention of ZrMg-NMC cathode was poor ($\approx 71\%$ after 100 cycles, $\approx 68\%$ after 200 cycles) during cycling within higher cutoff voltage $3 \leq V \leq 4.5$ V. This anomalous behavior was also observed with NMC cathode, wherein slightly lower sp. capacity has been observed at lower cutoff voltage, with better capacity retention.^[49] The long cycle test of ZrMg-NMC was carried out at 0.1C and 1C rates in two different potential windows (see Figure 6d). At 0.1C, the capacity fading slightly improved after 100 cycles, and sp. capacity of $\approx 76 \text{ mAhg}^{-1}$ ($3 \leq V \leq 4.5$ V) and $\approx 110 \text{ mAhg}^{-1}$ ($3 \leq V \leq 4.2$ V) was observed after 500 cycles. However, the capacity fading was severe during cycling at 1C, delivering sp. capacity of $\approx 42 \text{ mAhg}^{-1}$ ($3 \leq V \leq 4.5$ V) and $\approx 69 \text{ mAhg}^{-1}$ ($3 \leq V \leq 4.2$ V) after 500 cycles.

The electrochemical cycling behavior at two different potential windows has been further investigated by monitoring the evolution of charge/discharge curves. The charge/discharge curves of ZrMg-NMC cathode for 1st, 10th, and 100th cycles are shown in Figure 6e, f illustrate a sudden voltage drop to ≈ 4.2 V while cycling between $3 \leq V \leq 4.5$ V. The gradual voltage decay evident from 1st to 100th cycle while cycling within $3 \leq V \leq 4.5$ V occurs possibly due to surface reconstruction and formation of NiO-like phase, providing strong evidence in favor of cycling within a narrower potential window ($3 \leq V \leq 4.2$ V) to deliver a stable performance. Additionally, $H2 \rightarrow H3$ and $M \rightarrow H2$ phase transformation can be avoided during cycling within $3 \leq V \leq 4.2$ V, providing better structural integrity and preventing electrolyte decomposition.^[50-52] Overall, Zr and Mg codoping in NMC delayed the $H2 \rightarrow H3$ phase transformation, pushing it further at a higher voltage.

Further, the average discharge voltage was determined using the following formula: discharge voltage = energy density / discharge specific capacity (Figure S7, supporting information). The average discharge voltage of NMC falls rapidly from ≈ 3.65 to ≈ 3.54 V after 200 cycles, but ZrMg-NMC exhibits voltage decay from ≈ 3.7 V at 1st cycle to ≈ 3.64 V at 200th cycle while cycling the cathodes between $3 \leq V \leq 4.2$ V. Importantly, the Zr-NMC and Mg-NMC displayed better voltage retention than the NMC cathode. A similar trend was observed during charging-discharging between $3 \leq V \leq 4.5$ V, with individual or codoped samples performing better than NMC. The average voltage fading rate per cycle was also calculated and illustrated in Table S3, Supporting Information, revealing that ZrMg-NMC has superior

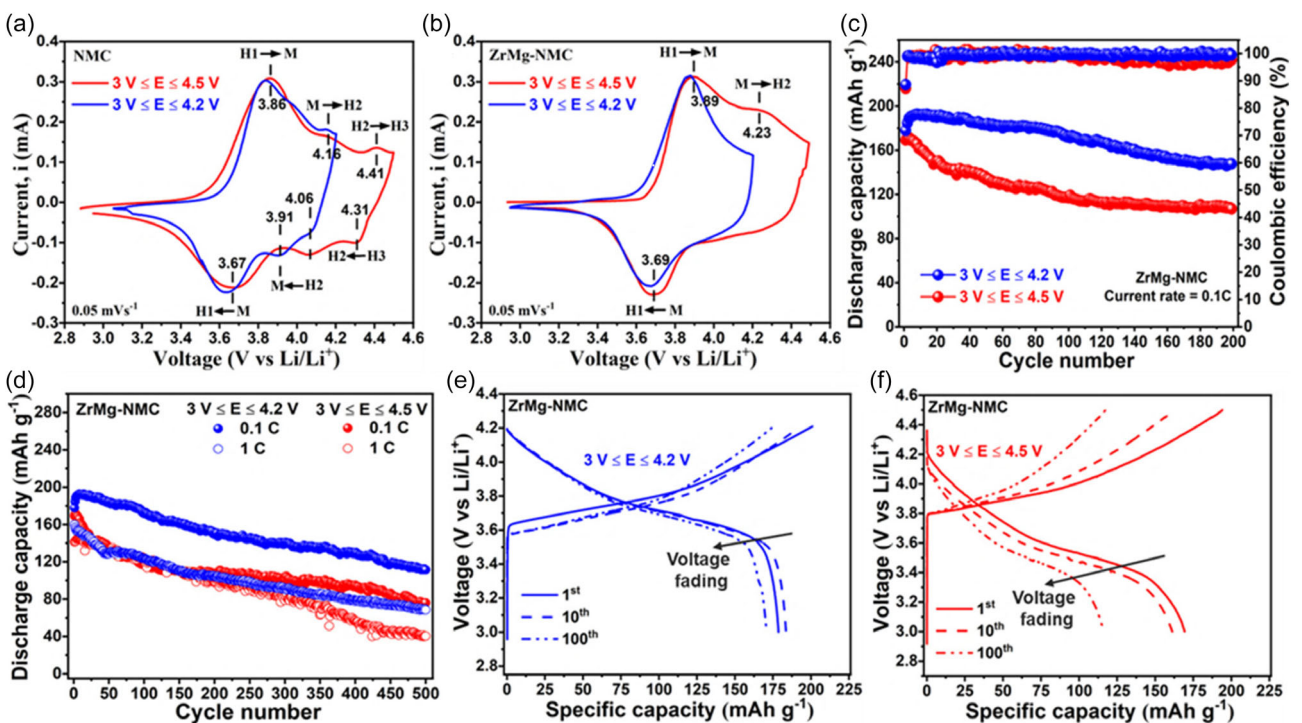


Figure 6. Cyclic voltammograms of a) NMC, b) ZrMg-NMC, c) cycle performance, and d) long-term cycling performance at 0.1C and 1C of ZrMg-NMC in different potential windows. Galvanostatic charge–discharge profile of 1st, 10th, and 100th cycles of ZrMg-NMC in e) $3 \text{ V} \leq E \leq 4.2 \text{ V}$ and f) $3 \text{ V} \leq E \leq 4.5 \text{ V}$ potential window.

voltage retention than any other cathodes due to the prevention of unwanted phase transformation during charging at higher voltage, as discussed before, irrespective of the charge–discharge voltage window.

Figure S8a,b, Supporting Information, shows the Nyquist plots and the equivalent Randle circuit of NMC, Zr-NMC, Mg-NMC, and ZrMg-NMC cathodes after 1st and 100th cycle in discharge state cycled within $3 \text{ V} \leq E \leq 4.5 \text{ V}$. The Nyquist plots consist of two semicircular arcs overlap with each other with an oblique line. The equivalent Randle circuit is represented as $[R_{\text{int}}(R_{\text{ct}}/\text{CPE1}) (R_{\text{SEI}}/\text{CPE2})W]$ where the individual terms are related to internal ohmic resistance (R_{int}), charge transfer resistance (R_{ct}), Warburg impedance (W), constant phase element (CPE), and SEI layer resistance (R_{SEI}), respectively. The arcs between the high-to-medium-frequency regions correspond to R_{int} and R_{ct} , while the oblique line at low frequency corresponds to Warburg diffusion phenomena (W) and low-frequency arc is related to R_{SEI} , respectively.^[53]

Table 2 shows the impedance parameters R_{int} , R_{SEI} , and R_{ct} obtained after curve-fitting, wherein NMC shows higher R_{ct} value of ≈ 560 and $\approx 1088 \Omega$ after 1st and 100th cycles, respectively, compared to ZrMg-NMC with R_{ct} values of ≈ 229 and $\approx 102.4 \Omega$, after 1st and 100th cycle, respectively. The R_{SEI} increased by $\approx 90.9 \Omega$ between 1st and 100th cycles for ZrMg-NMC cathode, which was increased by $\approx 286.2 \Omega$ for NMC cathode from 1st to 100th cycle. Additionally, the interfacial resistance variation (ΔR_{SEI}) of NMC and ZrMg-NMC was calculated $\approx 127.4\%$ and $\approx 30.8\%$, respectively, using an Equation (2)

$$\Delta R_{\text{SEI}} = \frac{R_{\text{SEI}-100\text{th}} - R_{\text{SEI}-1\text{st}}}{R_{\text{SEI}-1\text{st}}} \times 100 \quad (2)$$

where, $R_{\text{SEI}-1\text{st}}$ and $R_{\text{SEI}-100\text{th}}$ represents the R_{SEI} after 1st and 100th cycle, respectively. Thereby, it can be concluded that the codoping is favorable to minimize the ΔR_{SEI} .

Table 2. Impedance parameters determined from curve-fitting of Randle equivalent circuit in LIBs.

Cathode	Cycle	R_{int} [Ω]	R_{ct} [Ω]	Z_w	R_{SEI} [Ω]	Diffusion coefficient [cm ² s ⁻¹]
NMC	1st	≈ 22.37	≈ 560.2	0.0025	≈ 224.6	$\approx 8.2 \times 10^{-13}$
	100th	≈ 2.09	≈ 1088	0.0017	≈ 510.83	$\approx 3.1 \times 10^{-13}$
Zr-NMC	1st	≈ 13.81	≈ 550.4	0.0004	≈ 178.9	$\approx 5.9 \times 10^{-12}$
	100th	≈ 63.18	≈ 453.2	0.001	≈ 207.7	$\approx 3.3 \times 10^{-13}$
Mg-NMC	1st	≈ 15.67	≈ 490.1	0.0008	≈ 154.7	$\approx 4.3 \times 10^{-12}$
	100th	≈ 3.91	≈ 473.5	0.0061	≈ 505.1	$\approx 5.9 \times 10^{-13}$
ZrMg-NMC	1st	≈ 1.12	≈ 229.7	0.0027	≈ 294.5	$\approx 2.74 \times 10^{-12}$
	100th	≈ 5.87	≈ 102.4	0.0011	≈ 385.4	$\approx 1.7 \times 10^{-12}$

The galvanostatic intermittent titration technique (GITT) curves of NMC and ZrMg-NMC for 1st and 2nd cycle are shown in Figure 7a,d as a function of time, and corresponding Li-ion diffusion coefficient (D_{Li}) is calculated using Figure S9a–c, and Equation S3, Supporting Information.^[54–56] The GITT showed a remarkable difference in the iR drops between the 1st and 2nd cycles for NMC and ZrMg-NMC. The NMC cathode displayed a marked increase in iR drop, which is a function of the internal resistance between the 1st and 2nd cycles, leading to significant capacity fade compared to the ZrMg-NMC cathode. From the Figure 7b,e, it can be deduced that D_{Li} in the 2nd cycle was lower than that of the 1st cycle. This can be attributed to the increased charge transfer resistance between the cycles. During 1st charge, the D_{Li} of NMC and ZrMg-NMC was $\approx 9.88 \times 10^{-11} \text{ cm}^2 \text{ s}^{-1}$ and $\approx 3.84 \times 10^{-10} \text{ cm}^2 \text{ s}^{-1}$, respectively at $\approx 3.9 \text{ V}$. Similarly, the D_{Li} of NMC and ZrMg-NMC was $\approx 6.08 \times 10^{-11} \text{ cm}^2 \text{ s}^{-1}$ and $\approx 2.72 \times 10^{-10} \text{ cm}^2 \text{ s}^{-1}$, respectively, at $\approx 3.68 \text{ V}$ during 2nd discharge, which showed that codoping enhanced Li-ion diffusion by one order of magnitude during 1st and 2nd cycles. The gradual drop in D_{Li} at the end of the discharge cycle is attributed to the strong polarization of the cathodes and the lack of Li-ion vacancies for occupation, leading to strained diffusion behavior.^[57]

Akin to the diffusion coefficient, the internal resistance was also affected by the codoping into NMC. The internal resistance and the overpotential measure the voltage drop during a small halt in the current pulse, and the relaxation time reaches 30 min [Figure S9d,e, Supporting Information].^[58–60] Figure 7c,f show the internal resistance of ZrMg-NMC ($\approx 2462 \Omega$) was lower than the NMC ($\approx 3280 \Omega$) at $\approx 3.9 \text{ V}$ during 1st charge cycle, leading to a lower voltage drop. Similarly, the internal resistance of ZrMg-NMC ($\approx 1420 \Omega$) was lower than NMC ($\approx 2595 \Omega$) at $\approx 3.68 \text{ V}$ during 2nd discharge cycle.

Importantly, the internal resistance variation of ZrMg-NMC was lower than NMC, indicating less voltage decay during cycling.

X-ray absorption near-edge structure (XANES) spectra was performed to understand the electronic configuration of cathodes (Figure 8a). The transition metals K-edge spectra showed characteristic peaks of a layered and spinel structure with $R\bar{3}m$ and $Fd\bar{3}m$ space groups, respectively. This distinctive peak includes K-preedge absorption for $1s \rightarrow 3d$ excitation (peak A), and K-rising edge absorption for electric dipole-allowed $1s \rightarrow 4p$ transition with and without ligand-to-metal charge transfer (peaks B and C, respectively). The K-preedge absorption defines the ligand-field strength or spin state, and the K-rising edge absorption underscores the geometric structure or oxidation state,^[61–63] schematically represented through the energy diagram in Figure 8g. The minimal effect on pre-edge intensity-weighted average energy of pristine and doped NMC cathodes was due to charge on the metal affecting all energy levels equally. With doping, the Ni K-rising edge absorption peak in the ZrMg-NMC shifted to a higher energy band compared to pristine (Figure 8a) as the oxidation state was higher in the former and showed layered-like characteristics. The redox behavior of Ni K-edge spectra for NMC and ZrMg-NMC has been observed at pristine, charged, and discharged states (Figure 8b,c). The reference NiO spectra was included, indicating the Ni^{2+} oxidation state in Ni K-edge spectra. The energy shifts toward higher energy at the edge position with an increase in the oxidation state of Ni^{3+}/Ni^{4+} during charging to 4.5 V. In comparison, the curves shift toward lower energy with a reduction to Ni^{2+}/Ni^{3+} during discharge at 3.0 V. However, structural changes of the NMC cathode after 1st cycle show hardly any difference in the normalized intensity compared to ZrMg-NMC. The Fourier transformation of the XANES data was performed using Athena software to derive

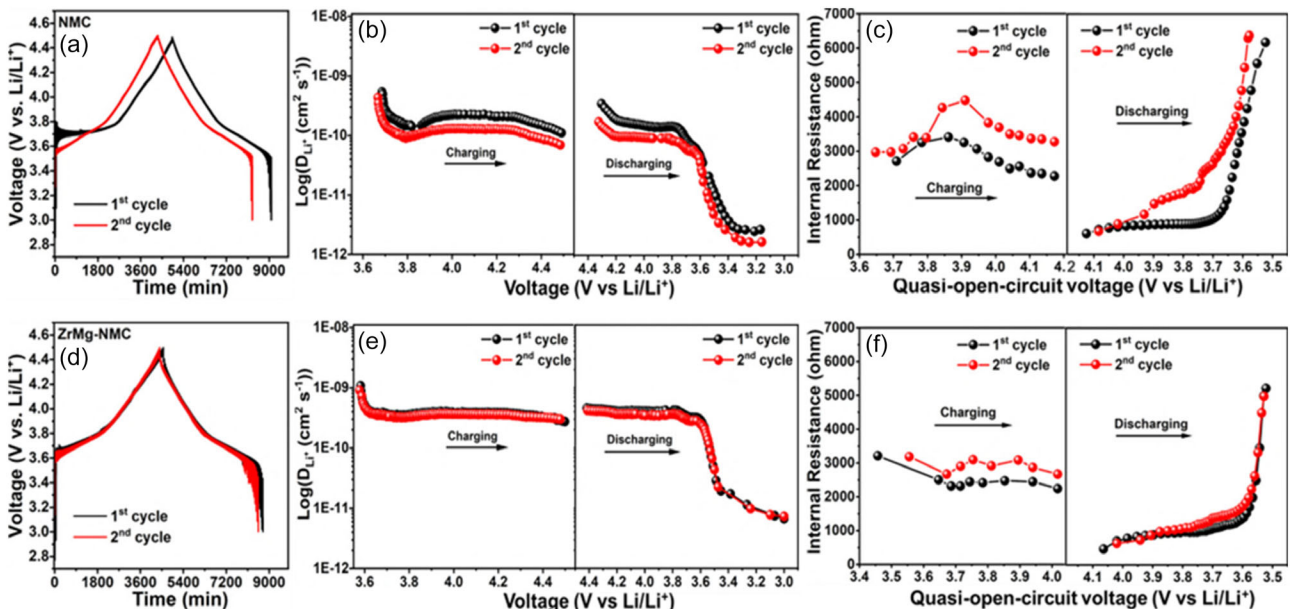


Figure 7. GITT profiles and calculated Li-ion diffusion coefficients (D_{Li}) and internal resistances during the 1st and 2nd cycles of a–c) NMC and d–f) ZrMg-NMC, respectively.

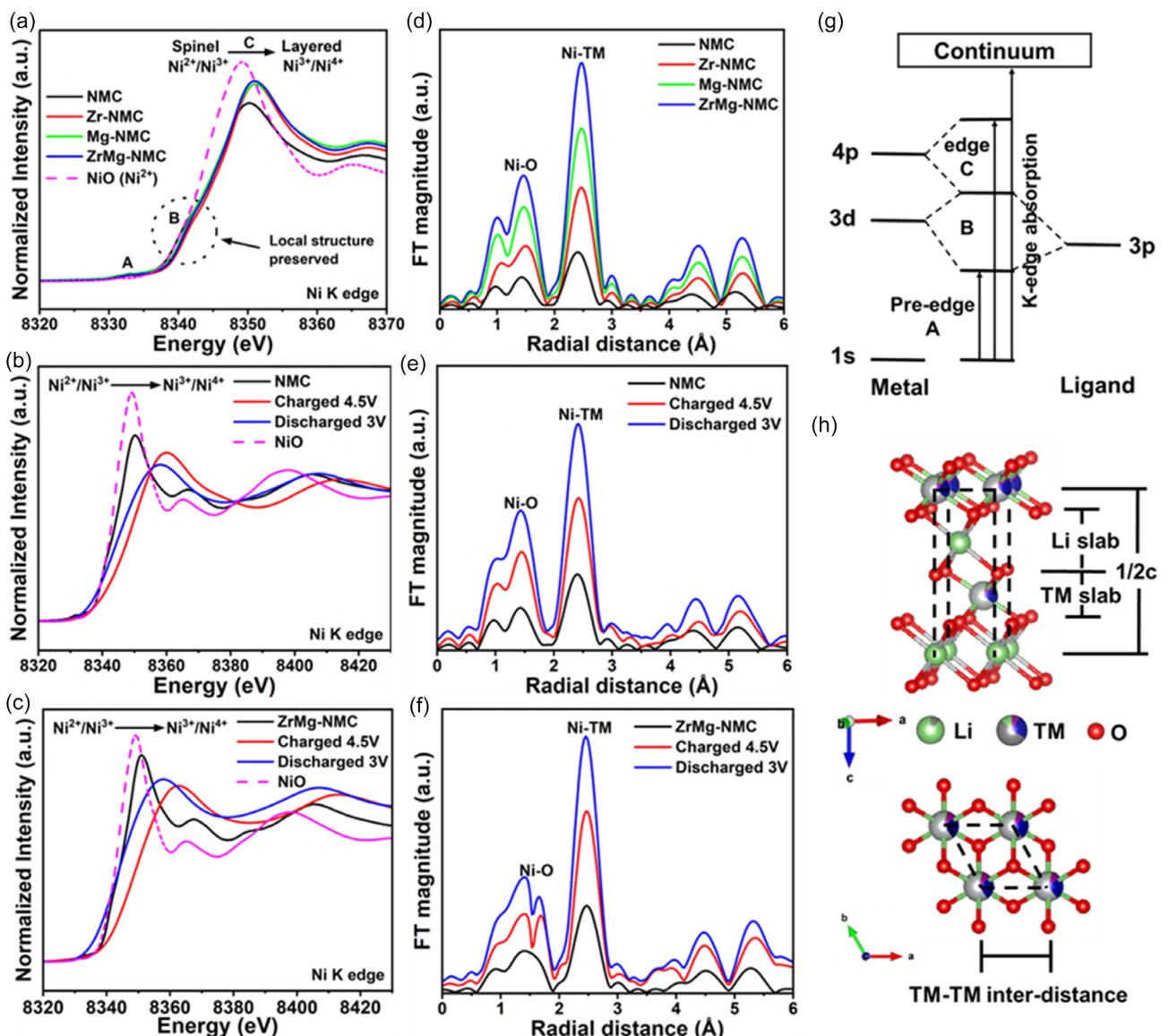


Figure 8. XANES spectra of a) Ni K-edge for all the prepared samples, Ni K-edge of b) NMC, and c) ZrMg-NMC during charging/discharging, d-f) RDF obtained by Fourier transform of XANES spectra, g) energy diagram representing the K-pre-edge and K-rising-edge absorption of T_M , and h) layered structure representation of a unit cell and corresponding bond length associated with T_M-T_M distance.

the radial distribution functions (RDF) for Ni K-edges at different state of charge, respectively (Figure 8d-f). The first peak between ≈ 1.1 – 1.8 Å defines the single scattering path of T_M –O (or Ni–O) by the nearest oxygen neighbor, and the second peak between ≈ 2.2 – 2.8 Å corroborates the single scattering path of T_M – T_M (or Ni– T_M) by the transition metals. The amplitude/maxima were higher for doped samples compared to pristine due to an increase in the c -axis length and unit cell volume, as previously mentioned. The bond lengths of both Ni–O and Ni– T_M in ZrMg-NMC exhibit remarkable change, increasing from ≈ 1.38 to ≈ 1.44 Å and ≈ 2.36 to ≈ 2.45 Å, respectively (Figure 8d), corresponding to change in the oxidation state of Ni and associated change in the Ni^{2+}/Ni^{3+} ratio (Figure 8a) owing to Zr and Mg codoping.^[64,65] Figure 8e, f shows the RDF and calculated bond lengths of Ni–O and Ni– T_M for NMC and ZrMg-NMC in pristine, charged, and discharged states, respectively. The Ni–O and

Ni– T_M bond lengths were reduced (≈ 1.32 Å and 2.29 Å, respectively) during charging from the pristine state and retained their original value (≈ 1.37 and ≈ 2.35 Å) during discharge for NMC. A similar trend was observed for ZrMg-NMC; however, the bond length of Ni–O and Ni– T_M (≈ 1.40 and 2.41 Å, respectively) was higher than NMC during charging as well as during discharge state (≈ 1.43 and ≈ 2.44 Å). The layered ($R\bar{3}m$) structure, as represented by a unit cell shown in Figure 8h, clearly shows that the lattice parameters a and c were dependent on LiO_6 and TMO_6 octahedra, respectively, wherein a was associated with T_M-T_M interlayer distance ($d_{T_M-T_M}$). The lattice parameter c was calculated using the formula $0.5c = 1.5(d_{Li\text{-slab}} + d_{TM\text{-slab}})$. Wang et al.^[66] reported that the T_M –O bond length determines the a and c lattice parameters. However, the XANES data show the T_M –O bond length increases due to the reduction to Ni^{2+} , with a higher c/a ratio observed for the doped samples compared to

the pristine, in agreement with the result obtained from the Rietveld refinement analysis (Figure 1c-d the structural degradation and capacity fading of the Ni-rich NMC cathodes developed herein. Therefore, postmortem analysis was performed on ZrMg-NMC cycled cathode to unveil the effect of codoping. Two types of cathodes were probed which cycled between potential windows of $3 \text{ V} \leq E \leq 4.5$ and $3 \text{ V} \leq E \leq 4.2$ V using ex situ XRD, FESEM, and XANES post 100 cycles in discharged state (Figure 9). The XRD pattern (Figure 9a) illustrates that the (003) peak intensity of ZrMg-NMC cathode remains intact upon cycling within $3 \text{ V} \leq E \leq 4.2$ V than $3 \text{ V} \leq E \leq 4.5$ V, suggesting that ZrMg-NMC cathode during cycling with a cutoff voltage 4.2 V retained layered structure with less cation disordering. The Ni K-edge XANES spectra of pristine and cycled ZrMg-NMC cathode in two different potential windows are displayed in Figure 9b,c, indicating that the Ni K-edge shifted toward higher binding energy [$3 \text{ V} \leq E \leq 4.5$ V window: pristine ≈ 8350.95 and cycled ≈ 8354.66 , and $3 \text{ V} \leq E \leq 4.2$ V window: pristine ≈ 8350.95 eV and cycled ≈ 8353.15 eV] owing to Ni^{2+} to Ni^{4+} oxidation. The cross-sectional FESEM images of NMC and ZrMg-NMC cathodes before and after 100 cycles are compared in Figure 9d-i. The FESEM images demonstrate the presence of lateral cracks causing contact loss between the active mass and the current collector due to lattice strain originating from repeated cycling. The crack length and width were severe during cycling at a larger potential window.

It has been widely believed for several years that doping of nickel-rich NMC cathodes can improve electrochemical properties, but a comprehensive understanding was lacking. Therefore, it was necessary to investigate and analyze the intrinsic mechanisms that are intricately involved to reveal the relationship between the single or the codoping effect of cations in terms of electrochemical performance (Table S4, Supporting Information). A comparison of the capacity retention of various doped NMC hitherto reported in the literature with Zr^{4+} and Mg^{2+} codoped $\text{LiNi}_{0.65}\text{Co}_{0.25}\text{Mn}_{0.1}\text{O}_2$ cathode shows that the latter demonstrates outstanding structural stability and capacity retention.

3. Conclusions

In conclusion, the incorporation of equimolar Mg^{2+} and Zr^{4+} -ions dual-site codoping in Ni-rich $\text{LiNi}_{0.65}\text{Co}_{0.25}\text{Mn}_{0.1}\text{O}_2$ (NMC) cathode elevates the electrochemical properties, minimizing unwanted $\text{H}_2\rightarrow\text{H}_3$ phase transformation, and enabling high voltage (≤ 4.5 V) operation in LIBs. The high-resolution TEM and XPS analysis disclose that calcined NMC particles surface was primarily composed of rhombohedral, spinel-like, and rock salt phases impairing high voltage charging that was drastically reduced in Zr-Mg codoped NMC sample promoting the formation of rhombohedral structure, with a higher Ni^{3+} ratio (ZrMg-NMC: $\approx 55.6\%$ and NMC: $\approx 49.8\%$) lowering antisite defects.

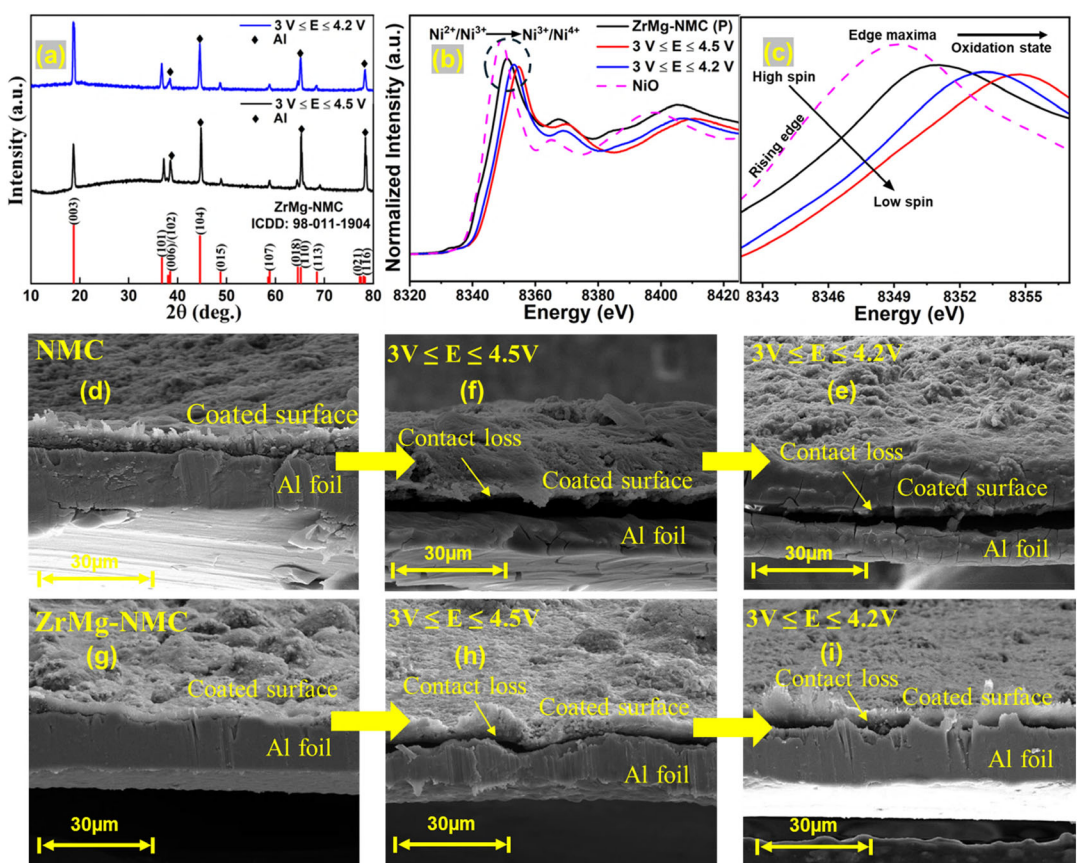


Figure 9. a) Ex situ XRD patterns, b) Ni K-edge XANES spectra, and c) corresponding magnified view of ZrMg-NMC cathode in a different potential window. The cross-sectional FESEM images of NMC and ZrMg-NMC cathode d,g) before cycled, f,h) in $3 \text{ V} \leq E \leq 4.5$ V, and e,i) in $3 \text{ V} \leq E \leq 4.2$ V potential window, respectively, after 100 cycles.

Additionally, codoping is able to arrest the gradual capacity and the voltage decay common for Ni-rich $\text{LiNi}_{0.65}\text{Co}_{0.25}\text{Mn}_{0.1}\text{O}_2$ cathode, improving electrochemical performance than pristine or heteroatom doped samples during standard (≤ 4.2 V) or high voltage (≤ 4.5 V) operation due to increasing interlayer spacing and Ni—O bond length preventing structural collapse as evidenced by ex situ XANES spectra and RDF analysis. This study provides an effective means to improve the high voltage performance of Ni-rich layered oxide cathode by carefully choosing higher valence cations with optimal concentration doped simultaneously in Li and T_{M} sites.

4. Experimental Section

Materials Synthesis

The layered oxide ($\text{Li}_{x}\text{Ni}_{1-y-z}\text{Mn}_y\text{Co}_z\text{O}_2$, $x = 1$, $y = 0.1$, and $z = 0.25$) cathode was synthesized by the coprecipitation route. Stoichiometric amounts of 0.65 mol nickel nitrate hexahydrate (Fisher Scientific, $\approx 99\%$), 0.25 mol cobalt nitrate hexahydrate (Fisher Scientific, $\approx 98.1\%$), and 0.1 mol manganese acetate tetrahydrate (Fisher Scientific, $\approx 98\%$) were taken as the precursor, while $\approx 6\%$ excess lithium hydroxide (Fisher Scientific, $\approx 99.8\%$) was utilized to compensate for the lithium loss during thermal treatment. Initially, the stoichiometric amount of the precursors was dissolved into deionized (DI) water and stirred for 30 min. An aqueous solution of ammonium hydroxide (NH_4OH) and sodium hydroxide (NaOH) was prepared at 2 M concentration and added to the precursor solution to maintain a pH of ≈ 11.5 . The precipitated $\text{Ni}_{0.65}\text{Mn}_{0.1}\text{Co}_{0.25}(\text{OH})_2$ [NMC(OH)₂] powder was centrifuged and washed with DI water until the pH became ≈ 7.0 . The precipitated NMC(OH)₂ was dried in a vacuum oven at 90 °C overnight and then ground thoroughly using agate mortar. The obtained NMC(OH)₂ was mixed with 1.06 moles of lithium hydroxide using agate mortar. The obtained powder was preheated at 450 °C for 5 h and again grounded thoroughly, followed by calcination at 850 °C for 12 h in a muffle furnace. The pristine and doped NMC powder with 0.01 mol of Zr^{4+} , 0.01 mol of Mg^{2+} , and codoped with 0.01 mol of Zr^{4+} and 0.01 mol of Mg^{2+} were synthesized by coprecipitation route under identical condition, and the samples were named as NMC, Zr-NMC, Mg-NMC, and ZrMg-NMC, respectively. The Zr^{4+} and Mg^{2+} codoped NMC was synthesized by mixing 0.01 mol zirconia with as-obtained 0.99 mol NMC(OH)₂ in an ethanol solution. The solution was centrifuged and dried in a vacuum oven at 90 °C overnight. The obtained Zr-doped NMC(OH)₂ was mixed with 1.06 mol lithium hydroxide and 0.01 mol magnesium acetate using an agate mortar. A similar heating procedure was followed, as mentioned above.

Materials Characterizations

The powder X-ray diffraction (XRD) patterns were collected with a Malvern Panalytical X-ray diffractometer model Empyrean in the 2θ range 10°–80° using CuK_{α} radiation with a step size of 5°/min. The Rietveld refinement was performed to extract the structural information and lattice parameter(s) of the powder samples by Thompson–Cox–Hastings pseudo-Voigt (with axial divergence asymmetry) function, refining the full-width at half-maximum, shape, background, atomic sites, site occupancy factor, and unit cell parameters using the FullProf software package. The vibrating sample magnetometer (VSM) was utilized to determine the temperature-dependent magnetic moment with temperature varying from 27 to 527 °C. The field emission scanning electron microscopy (FESEM) and energy dispersive spectroscopy (EDS) were performed using a Nova NanoSEM FEI450 operating at 15 kV system for morphological and elemental analysis, respectively. The high resolution transmission electron

microscopy (HR-TEM) images were recorded using an FEI TECNAI TF-30 G2. The FFT TEM images were analyzed using CrysTBox Server 1.10 software. The X-ray photoelectron spectroscopy (XPS) and X-ray absorption near edge structure (XANES) of pristine and doped cathodes were collected from the scanning XPS and EXAFS beamline (BL-14 and BL-09, respectively) at Indus-2 with a synchrotron radiation source (accelerated at 2.5 GeV having storage ring with bending magnets and using bent crystal (Si 111) monochromator or polychromator) at Raja Ramanna Centre for Advanced Technology (RRCAT) Indore, India. The XPS and XANES spectra were analyzed using CasaXPS 2.3.25 and Athena Demeter 0.9.26, respectively.

Electrochemical Measurement

The electrodes were assembled in CR2032 coin cells to investigate the electrochemical properties. The slurry was prepared by intimately mixing active material (80%), carbon black Super P-TIMCAL (10%), and polyvinylidene fluoride (PVDF, 10%) in n-methyl-2-pyrrolidone (NMP) solvent. The slurry was tape cast on an Al foil using a doctor blade with a target coating thickness of ≈ 37 μm and then dried at 60 °C for 3 h in a hot air oven. Consequently, electrodes were dried at 90 °C for 15 h in a vacuum oven to get rid of the moisture content. The coin cells were fabricated in an Ar-filled glove box (UniLab Pro, mBraun Inc. O_2 & $\text{H}_2\text{O} < 1$ ppm) with lithium metal used as a counter electrode, Celgard 2400 separator with ≈ 14 wt% LiPF_6 dissolved in a solution of ≈ 36.6 wt% EMC, ≈ 19.2 wt% EC, ≈ 19.3 wt% DMC, ≈ 8 wt% PC, and ≈ 1.8 wt% VC electrolyte (BASF, Purolyte 88 150). The cyclic voltammetry (CV) was conducted using an electrochemical workstation (PGSTAT204, Metrohm Autolab) within $3 \text{ V} \leq E \leq 4.2 \text{ V}$ and $3 \text{ V} \leq E \leq 4.5 \text{ V}$ potential windows at a scan rate of 0.05 mVs^{-1} . The galvanostatic charge–discharge measurement and rate performance were also carried out between two different potential windows of $3 \text{ V} \leq E \leq 4.2 \text{ V}$ and $3 \text{ V} \leq E \leq 4.5 \text{ V}$ (vs. Li^+/Li) at current rates of 0.1C, 0.2C, 0.5C, and 1C ($= 180 \text{ mA g}^{-1}$) using an Arbin battery tester (LBT series, Model 21084UC). The electrochemical impedance spectroscopy (EIS) was performed within the frequency range of 0.1 Hz to 100 kHz. The spectra were obtained with 5 mV potentiostat signal amplitude and analyzed using ZView software. The galvanostatic intermittent titration technique (GITT) was performed during the 1st and 2nd cycles at a current rate of 0.1C within $3 \text{ V} \leq E \leq 4.5 \text{ V}$ using a current pulse of 10 min, followed by a relaxation time of 30 min each.

Acknowledgements

A.K. and P.S. planned the work. P.S. acquired the external funding from DST Nanomission (grant no. DST/NM/NT/2018/176) for carrying out the research. A.K. is indebted to UKG for performing the XPS and XANES analysis at Indus-2, Beamline-9 and 14, RRCAT Indore, India. R.M. helped to analyze the data.

Conflict of Interest

The authors declare no conflict of interest.

Author Contributions

Abhishek Kumar: data curation (lead); formal analysis (equal); investigation (lead); methodology (lead); validation (lead); writing—original draft(lead). **Uttam Kumar Goutam:** data curation (supporting); formal analysis (supporting); investigation

(supporting); resources (supporting). **Ranabrata Mazumder**: formal analysis (supporting); supervision (supporting); validation (supporting); writing—review & editing (supporting). **Partha Saha**: conceptualization (lead); formal analysis (equal); funding acquisition (lead); project administration (lead); supervision (lead); validation (equal); writing—review & editing (equal).

Data Availability Statement

The data that support the findings of this study are available from the corresponding author upon reasonable request.

Keywords: cathode · cation mixing · dopings · layered oxides · lithium batteries

- [1] J. B. Goodenough, Y. Kim, *Chem. of Mater.* **2010**, *22*, 587.
- [2] H. Kang, Y. Liu, K. Cao, Y. Zhao, L. Jiao, Y. Wang, H. Yuan, *J. Mater. Chem. A* **2015**, *3*, 17899.
- [3] A. Khaligh, Z. Li, *IEEE Transactions on Vehicular Technol.* **2010**, *59*, 2806.
- [4] E. Schatzl, A. Khaligh, P. O. Rasmussen, *IEEE Trans. Veh. Technology* **2009**, *58*, 3882.
- [5] C. Zhu, P. Yang, D. Chao, W. Mai, H. J. Fan, *Chem. Nano. Mat* **2015**, *1*, 458.
- [6] W.-J. Ge, X. Li, H. Wang, W. Li, A.-J. Wei, G.-C. Peng, M.-Z. Qu, *J. Alloys and Compounds* **2016**, *684*, 594.
- [7] A. Manthiram, *Nat. Commun.* **2020**, *11*, 1.
- [8] Z. Yang, W. Qin, J. Liu, Y. Liu, *Solid State Sci.* **2022**, *125*, 106840.
- [9] W. Liu, P. Oh, X. Liu, M. J. Lee, W. Cho, S. Chae, Y. Kim, J. Cho, *Angew. Chem. Int. Ed.* **2015**, *54*, 4440.
- [10] X. Huang, Q. Qiao, Y. Sun, F. Li, Y. Wang, S. Ye, *J. Solid State Electrochem.* **2015**, *19*, 805.
- [11] S. S. Zhang, *Energy Storage Mater.* **2020**, *24*, 247.
- [12] T. Li, X.-Z. Yuan, L. Zhang, D. Song, K. Shi, C. Bock, *Electrochem. Energy Rev.* **2020**, *3*, 43.
- [13] A. Saha, S. Taragin, Rosy, S. Maiti, T. Kravchuk, N. Leifer, M. Tkachev, M. Noked, *Small* **2022**, *18*, 2104625.
- [14] J. Yang, Y. Xia, *ACS Appl. Mater. Interfaces* **2016**, *8*, 1297.
- [15] X. Liu, S. Wang, L. Wang, K. Wang, X. Wu, P. Zhou, Z. Miao, J. Zhou, Y. Zhao, S. Zhuo, *J. Power Sources* **2019**, *438*, 227017.
- [16] Y. Lv, X. Cheng, W. Qiang, B. Huang, *J. Power Sources* **2020**, *450*, 227718.
- [17] Y. Huang, B. Zhang, J. Zhang, Y. Wang, L. Xia, M. Xiang, W. Han, J. Li, Z. Feng, Y. Liu, *Small* **2025**, 2410999.
- [18] Y. Cho, P. Oh, J. Cho, *Nano Lett.* **2013**, *13*, 1145.
- [19] G. Sun, X. Yin, W. Yang, A. Song, C. Jia, W. Yang, Q. Du, Z. Ma, G. Shao, *Phys. Chem. Chem. Phys.* **2017**, *19*, 29886.
- [20] F. Schipper, E. M. Erickson, C. Erk, J.-Y. Shin, F. F. Chesneau, D. Aurbach, *J. Electrochem. Society* **2016**, *164*, A6220.
- [21] L. Liang, X. Sun, C. Wu, L. Hou, J. Sun, X. Zhang, C. Yuan, *ACS Appl. Mater. Interfaces* **2018**, *10*, 5498.
- [22] E. Williams, E. Kendrick, *Electrochemical Society Meeting Abstracts* **244**, The Electrochem. Society, Inc. **2023**, pp. 225–225, <https://doi.org/10.1149/MA2023-022225mtgabs>.
- [23] Y. Chen, Y. Li, W. Li, G. Cao, S. Tang, Q. Su, S. Deng, J. Guo, *Electrochimica Acta* **2018**, *281*, 48.
- [24] W. Yan, S. Yang, Y. Huang, Y. Yang, G. Yuan, *J. Alloys Compd.* **2020**, *819*, 153048.
- [25] T. Weigel, F. Schipper, E. M. Erickson, F. A. Susai, B. Markovsky, D. Aurbach, *ACS Energy Lett.* **2019**, *4*, 508.
- [26] J. Wang, Y. Nie, C. Miao, Y. Tan, M. Wen, W. Xiao, *J. Colloid Interface Sci.* **2021**, *601*, 853.
- [27] L. Li, E. Han, L. Zhu, S. Qiao, C. Du, H. Liu, *Solid State Ionics* **2020**, *346*, 115220.
- [28] T. Sattar, S.-H. Lee, S.-J. Sim, B.-S. Jin, H.-S. Kim, *Int. J. Hydrogen Energy* **2020**, *45*, 19567.
- [29] J. Zhang, F. Wu, X. Dai, Y. Mai, Y. Gu, *ACS Sustainable Chem. Eng.* **2021**, *9*, 1741.
- [30] Z. Ye, B. Zhang, T. Chen, Z. Wu, D. Wang, W. Xiang, Y. Sun, Y. Liu, Y. Liu, J. Zhang, *Angew. Chem. Int. Ed.* **2021**, *60*, 23248.
- [31] M. Zubair, M. I. Khan, M. K. Tufail, M. F. Iqbal, M. M. Fadhal, A. Hassan, H. S. Abd-Rabboh, T. Alshahrani, H. Ali, M. R. Khan, *Ceram. Int.* **2022**.
- [32] F. Schipper, H. Bouzaglo, M. Dixit, E. M. Erickson, T. Weigel, M. Talianker, J. Grinblat, L. Burstein, M. Schmidt, J. Lampert, C. Erk, B. Markovsky, D. T. Major, D. Aurbach, *Adv. Energy Mater.* **2018**, *8*, 1701682.
- [33] B. Jeevanantham, M. Shobana, *J. Energy Storage* **2022**, *54*, 105353.
- [34] F. Wu, J. Tian, Y. Su, J. Wang, C. Zhang, L. Bao, T. He, J. Li, S. Chen, *ACS Appl. Mater. Interfaces* **2015**, *7*, 7702.
- [35] K. Shaju, G. S. Rao, B. Chowdari, *Electrochimica Acta* **2002**, *48*, 145.
- [36] W. Yang, H. Li, D. Wang, C. Xu, W. Xiang, Y. Song, F. He, J. Zhang, B. Zheng, B. Zhong, *Nano Energy* **2022**, *104*, 107880.
- [37] L. Yin, Z. Li, G. S. Mattei, J. Zheng, W. Zhao, F. Omenya, C. Fang, W. Li, J. Li, Q. Xie, *Chem. Mater.* **2019**, *32*, 1002.
- [38] N. Kosova, E. Devyatkina, V. Kaichev, *J. Power Sources* **2007**, *174*, 965.
- [39] X. Zhang, W. Jiang, A. Mauger, F. Gendron, C. Julien, *J. Power Sources* **2010**, *195*, 1292.
- [40] R. Wang, Q. Li, F. Wang, J. Ding, B. An, J. Ruan, D. Sun, F. Fang, F. Wang, *Small* **2024**, *20*, 2400762.
- [41] T. Hölderle, M. Monchak, V. Baran, O. Dolotko, S. Bette, D. Mikhailova, A. Voss, M. Avdeev, H. Ehrenberg, P. Müller-Buschbaum, *J. Power Sources* **2023**, *564*, 232799.
- [42] U.-H. Kim, S.-T. Myung, C. S. Yoon, Y.-K. Sun, *ACS Energy Lett.* **2017**, *2*, 1848.
- [43] L. Zhu, T.-F. Yan, D. Jia, Y. Wang, Q. Wu, H.-T. Gu, Y.-M. Wu, W.-P. Tang, *J. Electrochem. Society* **2019**, *166*, A5437.
- [44] Y. Liang, S. Li, J. Xie, L. Yang, W. Li, C. Li, L. Ai, X. Fu, X. Cui, X. Shangguan, *New J. Chem.* **2019**, *43*, 12004.
- [45] X. Song, G. Liu, H. Yue, L. Luo, S. Yang, Y. Huang, C. Wang, *Chem. Eng. J.* **2021**, *407*, 126301.
- [46] C. R. Birk, M. R. Roberts, E. McTurk, P. G. Bruce, D. A. Howey, *J. Power Sources* **2017**, *341*, 373.
- [47] S. K. Sharma, G. Sharma, A. Gaur, A. Aray, F. S. Mirsafi, R. Abolhassani, H.-G. Rubahn, J.-S. Yu, Y. K. Mishra, *Energy Adv.* **2022**.
- [48] F. Schipper, H. Bouzaglo, M. Dixit, E. M. Erickson, T. Weigel, M. Talianker, J. Grinblat, L. Burstein, M. Schmidt, J. Lampert, *Adv. Energy Mater.* **2018**, *8*, 1701682.
- [49] Y. Ruan, X. Song, Y. Fu, C. Song, V. Battaglia, *J. Power Sources* **2018**, *400*, 539.
- [50] C. Xu, P. J. Reeves, Q. Jacquet, C. P. Grey, *Adv. Energy Mater.* **2021**, *11*, 2003404.
- [51] J. B. Adamo, A. Manthiram, *Chem. of Mater.* **2024**, *36*, 6226.
- [52] J. B. Adamo, A. Manthiram, *ACS Appl. Energy Mater.* **2025**.
- [53] N. Cogger, N. Evans, *An Introduction to Electrochemical Impedance Measurement*, Solarton Ltd., Farnborough, UK **1999**.
- [54] H. Liu, Z. Xie, W. Qu, E. Dy, S. Niketic, S. Brueckner, K. Tsay, E. Fuller, C. Bock, N. Zaker, *Small* **2022**, *18*, 2200627.
- [55] Y. Yang, H. Deng, L. Liu, J. Pan, P. Chen, Z. Shi, *J. Power Sources* **2024**, *616*, 235082.
- [56] J. Sun, B. Wen, Y. Li, H. Wang, M. De Volder, *Small* **2025**, 2410149.
- [57] L. Dashairya, V. Chaturvedi, A. Kumar, T. R. Mohanta, M. Shelke, P. Saha, *Solid State Ionics* **2023**, *396*, 116243.
- [58] J. Kim, S. Park, S. Hwang, W.-S. Yoon, *J. Electrochem. Sci. Technol.* **2022**, *13*, 19.
- [59] R. Xu, D. Wang, G. Yan, J. Duan, H. Guo, J. Wang, Z. Wang, X. Li, G. Li, *J. Energy Storage* **2023**, *70*, 108100.
- [60] R. Xu, X. Li, S. Tang, Z. Wang, H. Guo, W. Peng, D. Wang, J. Duan, J. Wang, G. Yan, *Appl. Energy* **2024**, *371*, 123630.
- [61] H. Kim, M. G. Kim, H. Y. Jeong, H. Nam, J. Cho, *Nano Lett.* **2015**, *15*, 2111.
- [62] A. Choi, J. Lim, H. J. Kim, S. C. Jung, H. W. Lim, H. Kim, M. S. Kwon, Y. K. Han, S. M. Oh, K. T. Lee, *Adv. Energy Mater.* **2018**, *8*, 1702514.
- [63] J. Kowalska, S. DeBeer, *Biochim. Biophys. Acta BBA-Mol. Cell Res.* **2015**, *1853*, 1406.
- [64] M. N. Ates, S. Mukerjee, K. Abraham, *RSC Adv.* **2015**, *5*, 27375.
- [65] G.-L. Xu, R. Amine, Y.-F. Xu, J. Liu, J. Gim, T. Ma, Y. Ren, C.-J. Sun, Y. Liu, X. Zhang, *Energy Environ. Sci.* **2017**, *10*, 1677.
- [66] D. Wang, C. Xin, M. Zhang, J. Bai, J. Zheng, R. Kou, J. Y. Peter Ko, A. Huq, G. Zhong, C.-J. Sun, *Chem. Mater.* **2019**, *31*, 2731.

Manuscript received: April 7, 2025

Revised manuscript received: May 17, 2025

Version of record online: